

A review of wavelet denoising in MRI and ultrasound brain imaging

Aleksandra Pižurica, Alle Meije Wink, Ewout Vansteenkiste,
Wilfried Philips and Jos B.T.M. Roerdink

Abstract—There is a growing interest in using multiresolution noise filters in a variety of medical imaging applications. We review recent wavelet denoising techniques for medical ultrasound and for magnetic resonance images and discuss some of their potential applications in the clinical investigations of the brain. Our goal is to present and evaluate noise suppression methods based on both image processing and clinical expertise.

We analyze two types of filters for magnetic resonance images (MRI): noise suppression in magnitude MRI images and denoising blood oxygen level-dependent (BOLD) response in functional MRI images (*fMRI*). The noise distribution in magnitude MRI images is Rician, while the noise distribution in BOLD images has been recently shown to follow a Gaussian model well. We evaluate different methods based on signal to noise ratio improvement and based on the preservation of the shape of the activated regions in *fMRI*.

A critical view on the problem of speckle filtering in ultrasound images is given where we discuss some of the issues that are overlooked in many speckle filters like the relevance of the “speckled texture”, expert-defined features of interest and the reliability of the common speckle models. We analyze the use of multiresolution speckle filters to improve the automatic processing steps in the clinical research of non-cystic periventricular leukomalacia. In particular we apply speckle filters to ultrasound neonatal brain images and we evaluate the influence of the filtering on the effectiveness of the subsequent classification and segmentation of flairs of affected tissue in comparison with the manual delineation of clinicians.

Index Terms—Image denoising, wavelets, magnetic resonance imaging, ultrasound, statistical parametric mapping, false discovery rate control

I. INTRODUCTION

The rapid development of medical imaging technology and the introduction of new imaging modalities, such as functional magnetic resonance imaging (*fMRI*), calls for new image processing methods including specialized noise filtering, enhancement, classification and segmentation techniques. This paper reviews some of the recent multiresolution denoising methods for medical ultrasound and MRI imaging and their applications in some clinical investigations of the human brain. We try to present an objective and critical discussion of several representative, recent noise filters based on their performance in a controlled environment (simulations) as well as in practical

A. Pižurica, E. Vansteenkiste and W. Philips are with the Department for Telecommunications and Information Processing (TELIN), Ghent University, Sint-Pietersnieuwstraat 41, B-9000 Gent, Belgium.

A.M. Wink is with the Brain Mapping Unit, Department of Psychiatry, Addenbrooke’s Hospital, University of Cambridge, Hills Road, Cambridge CB2 2QQ, United Kingdom.

J. B.T.M. Roerdink is with the Institute for Mathematics and Computing Science, University of Groningen, P.O. Box 800, 9700 AV Groningen, The Netherlands.

real-life imaging cases.

Contrasting many imaging applications (like commercial broadcast) where the quality of the denoised image is evaluated by how well it pleases the human eye, medical applications impose other priorities, where for example smoothing of “features of interest” is intolerable as well as the generation of artifacts that could be misinterpreted as clinically interesting features. We stress the importance of such conditions and formulate some requirements that medical noise filters need to meet in order to be of better assistance in real clinical investigations.

A practical ultrasound imaging application that we address is the semi-automatic segmentation of flares in ultrasound brain imaging of *Periventricular Leukomalacia* (PVL). We evaluate noise suppression based on both image processing and clinical expertise. The latter by using delineations of the affected brain regions that are made manually by medical doctors. The *fMRI* application that we consider is the detection and the classification of activated brain regions by using the widely used statistical parametric mapping. In this application we evaluate and discuss the usefulness of different noise reduction methods.

A. Paper structure

The structure of this paper is as follows. The Introductory Section ends with a brief review of wavelet transforms and wavelet denoising principles.

Section II addresses speckle noise reduction in ultrasound images. We start with a description of the speckle noise model (Sec. II-A) and we give an overview of some of the well-adopted single- and multiresolution speckle filters (Sec. II-B). Next we define and discuss some criteria that are important for designing a reliable noise filter in real, clinical applications (Sec. II-C) and we present, in more detail, one recent technique that complies with such requirements (Sec. II-D).

In Section III we analyze the use of speckle filtering in the clinical studies of non cystic PVL. First we introduce the analyzed imaging application (Sec. III-A) and we review the existing methods for the (semi-)automatic segmentation of the affected regions (Sec. III-B). Based on multiple experiments and taking into account the expert-defined ground truth, we investigate the effect of wavelet denoising on the segmentation accuracy (Sec. III-C) and on the segmentation reproducibility (Sec. III-D) to end with the conclusions in Sec. III-E.

In Section IV we address the denoising of MRI image magnitude, giving a brief description of the noise statistics (Sec. IV-A) and presenting a practical denoising algorithm (Sec. IV-B). Section V is devoted to *fMRI*, where we analyze a number of wavelet-based denoising schemes

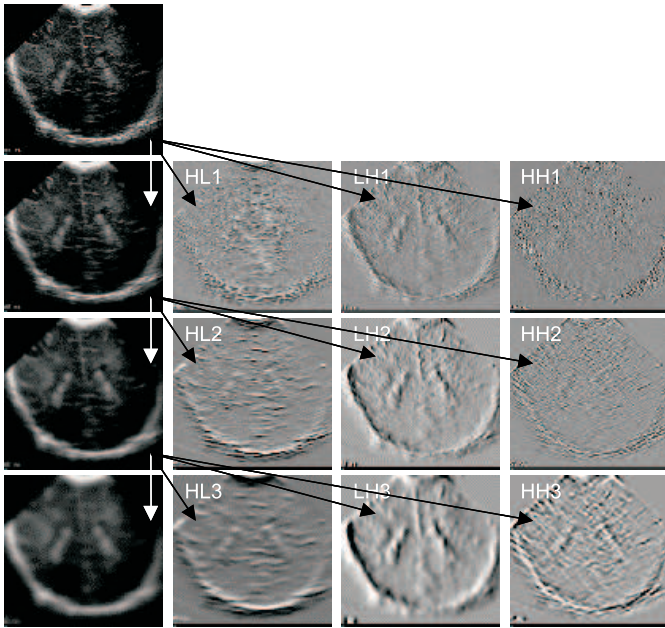


Fig. 1. An illustration of the non-decimated wavelet transform. Left column: approximation subbands. HL_i , LH_i and HH_i are the horizontal, vertical and diagonal detail subbands at the resolution level i .

experimentally. First we describe common f MRI analysis methods (Sec. V-A) and we choose a representative set of wavelet denoising schemes (Sec. V-B). We perform the experiments on artificial blood oxygen level-dependent (BOLD) images (Sec. V-C) and on real f MRI time series data (Sec. V-D). A discussion on this topic is in Sec. V-E and a general conclusion of the paper is in Section VI.

B. Wavelet domain noise filtering

The discrete wavelet transform [1–3] translates the image content into an *approximation* subband and a set of *detail* subbands at different orientations and resolution scales. Typically, the band-pass content at each scale is divided into three orientation subbands characterized by horizontal, vertical and diagonal directions. The approximation subband consists of the so-called *scaling* coefficients and the detail subbands are composed of the *wavelet* coefficients. Here we consider a *non-decimated* wavelet transform [2] where the number of the wavelet coefficients is equal at each scale.

Fig. 1 shows a non-decimated wavelet decomposition of an ultrasound image. In the detail subbands HL_i , LH_i and HH_i , the brightest color represents large positive values of the wavelet coefficients and the dark color corresponds to the negative coefficient values with largest magnitudes. Several properties of the wavelet transform, which make this representation attractive for denoising, are easily recognized in Fig. 1:

- *multiresolution* - image details of different sizes are analyzed at the appropriate resolution scales
- *sparsity* - the majority of the wavelet coefficients are small in magnitude
- *edge detection* - large wavelet coefficients coincide with image edges

- *edge clustering* - the “edge” coefficients within each subband tend to form spatially connected clusters
- *edge evolution across scales* - the coefficients that represent image edges tend to persist across the scales

Wavelets have been used for denoising in many medical imaging applications [4–12]. A general procedure is: (i) calculate the discrete wavelet transform; (ii) remove noise from the wavelet coefficients and (iii) reconstruct a denoised signal or image by applying the inverse wavelet transform. The *scaling* coefficients are typically not modified except for some special imaging modalities like MRI that we address later. The noise-free component of a given wavelet coefficient is typically estimated by *wavelet shrinkage* [13] the idea of which is to heavily suppress those coefficients that represent noise and to retain the coefficients that are more likely to represent the actual signal or image discontinuities.

Let $w_{k,j}^D$ represent the wavelet coefficient at the resolution scale 2^j ($1 \leq j \leq J$), spatial position k and orientation D . For compactness, we shall omit the indices that denote the scale and the orientation unless in cases where it is explicitly needed. Assume that in each wavelet subband an additive noise model holds

$$w_k = y_k + n_k \quad (1)$$

where y_k is the unknown noise-free signal component and n_k an arbitrary noise contribution. A majority of the wavelet shrinkage estimators can be represented as

$$\hat{y}_k = R_k w_k, \quad 0 \leq R_k \leq 1 \quad (2)$$

where R_k denotes a *shrinkage factor*. Ideally, R_k should be close to zero when w_k is likely to represent pure noise and it should be close to one when w_k is likely to represent a true signal or image discontinuity. For the classical wavelet thresholding rules [13–16] a threshold value T is defined and $R_k = 0$ is specified as follows. For *hard thresholding*: $R_k = 0$ if $|w_k| < T$ and $R_k = 1$ if $|w_k| \geq T$. For *soft-thresholding*: $R_k = 0$ if $|w_k| < T$ and $R_k = 1 - T/|w_k|$ if $|w_k| \geq T$. One of the first soft-thresholding methods was developed within *medical imaging*, for the noise reduction in magnetic resonance images [17].

Wavelet-based denoising methods have also been developed within a *Bayesian* framework [18–27] also used in medical imaging [10–12]. Examples of Bayesian wavelet domain estimators of the form (2) are the maximum a posteriori estimator under the Laplacian prior [28] (which essentially amounts to a soft thresholding) and locally adaptive linear minimum mean squared error estimators [29,30] where $R_k = \hat{\sigma}_k^2 / (\hat{\sigma}_k^2 + \sigma_n^2)$ and where σ_n denotes the noise standard deviation and $\hat{\sigma}_k$ denotes the estimate of the standard deviation of the signal (within a given local window centered at position k). A related, but more sophisticated approach is recently proposed in [31]. In some other approaches [32–34] R_k is defined as a probability that w_k represents a significant signal component under a *Markov random field* prior on the noise-free wavelet coefficients. Related methods that are based on *hidden Markov tree* models include [35–37].

II. NOISE REDUCTION IN ULTRASOUND IMAGES

A. Speckle noise in ultrasound images

Speckle noise [38,39] affects all coherent imaging systems including medical ultrasound. Within each resolution cell a number of elementary scatterers reflect the incident wave towards the sensor. The backscattered coherent waves with different phases undergo a constructive or a destructive interference in a random manner. The acquired image is thus corrupted by a random granular pattern, called *speckle*, that hinders the interpretation of the image content.

A speckled image $\mathbf{v} = \{v_1, \dots, v_n\}$ is commonly modelled as [7, 10]

$$v_i = f_i \vartheta_i, \quad (3)$$

where $\mathbf{f} = \{f_1, \dots, f_n\}$ is a noise-free ideal image, and $\vartheta = \{\vartheta_1, \dots, \vartheta_n\}$ is a unit mean random field. Modelling the correlated ultrasound speckle is studied in [39]. Some authors assume that realistic spatially correlated speckle noise in ultrasound images can be simulated by lowpass filtering a complex Gaussian random field and taking the magnitude of the filtered output [7, 10, 12].

B. Speckle filters

Some of the best known standard despeckling filters are the methods of *Lee* [40], *Frost* [41] and *Kuan* [42]. These filters use the second-order sample statistics within a minimum mean squared error estimation approach. More recent speckle filters in the image domain like the so-called *enhanced Lee* and the *enhanced Frost* filters [43] combine the filtering with a preliminary classification step: the image pixels are first assigned into one of the three classes: homogeneous, weakly textured or highly heterogeneous. Supposedly homogeneous image segments are simply averaged, while the highly heterogeneous ones are kept unmodified; only the remaining image segments (weakly textured) are adaptively filtered. Another common despeckling approach is the *homomorphic* Wiener filter where the image is first subjected to a logarithmic transform and then filtered with an adaptive filter for additive Gaussian noise. Other speckle filters include *morphological* methods [44]. Studies that compare different speckle filters in the image domain and in the wavelet domain usually show that wavelet domain filters are able to better preserve image details. [45]

Most of the wavelet domain speckle suppression methods apply first the logarithmic transformation. Assuming a purely multiplicative speckle model (II-A) these approaches simplify that the logarithmic operation transforms speckle into additive Gaussian noise. The transformed image is then typically denoised by wavelet thresholding [46,47] or by a Bayesian wavelet shrinkage [10] which relies on prior distributions for noise-free data. It should be noted that medical ultrasound devices often include some internal data preprocessing like a logarithmic compression of the dynamic range of the data. Noise in the resulting images is not purely multiplicative and an additional logarithmic transformation prior to speckle filtering seems less appropriate. Alternative speckle filters, that *do not* filter the image logarithm include a simple, edge-detection based method of [7] and a Maximum a Posteriori (MAP) estimator of [48].

C. Some notes on filtering medical ultrasound images

In developing an efficient and robust denoising method for medical ultrasound images one has to take into account the following

- *Adaptation to expert defined features of interest.* - For an experienced radiologist, speckle noise, which is in medical literature also referred to as “texture” [39], may present useful diagnostic information [49, 50]. The desired degree of speckle smoothing should ideally depend on the expert’s knowledge and on the application at hand like the enhancement for visual inspection or a preprocessing for an automatic segmentation. For an automatic segmentation it is usually preferred to keep the sharpness of the boundaries between different image regions and to smooth out the speckled texture. For a visual interpretation smoothing the texture may be less desirable.
- *Adaptation to spatial context.* - In most “natural” images including the medical ultrasound images there typically exist a significant spatial correlation. A spatially adaptive denoising can be based on statistical context models like Markov random fields [51] or simply on adapting certain filter parameters based on measurements from a local window around each pixel.
- *A critical view on the used noise models.* - A majority of the speckle filters assume fully developed speckle which is modelled as a multiplicative noise and often simplify that a logarithmic operation transforms speckle into additive white Gaussian noise. Such a speckle model seems to be too simplistic in the case of medical ultrasound images for different reasons. Speckle is not necessarily fully developed and there exist a pronounced spatial correlation. Moreover, the ultrasound devices themselves usually perform a preprocessing of the raw data including even a logarithmic compression. Thus in the displayed medical ultrasound images the noise differs significantly from the often assumed multiplicative model.

D. Filtering adopted to expert-defined features of interest

Clinicians usually tend to prefer the original noisy ultrasound images rather than the smoothed versions because the filters, no matter how sophisticated they are, can destroy some relevant image details. However, it is also true that noise suppression in many cases significantly enhances the visibility of some image features and it undoubtedly facilitates automatic image processing tasks such as segmentation. It is thus important to develop such noise filters, which can guarantee the preservation of those features that are of interest to the clinician.

D.1 *GenLik* method - an overview

A multiresolution denoising method that meets the requirements from Sec. II-C is, e.g., the method of [12] that will be called hereafter *GenLik* for it uses a Generalized Likelihood ratio formulation [52]. This method is very conservative in terms of the assumptions made - it assumes only that the image features of interest propagate well across scales but apart from that imposes no particular prior statistics on the signal and noise. The signal and noise statistics are in this method estimated from the

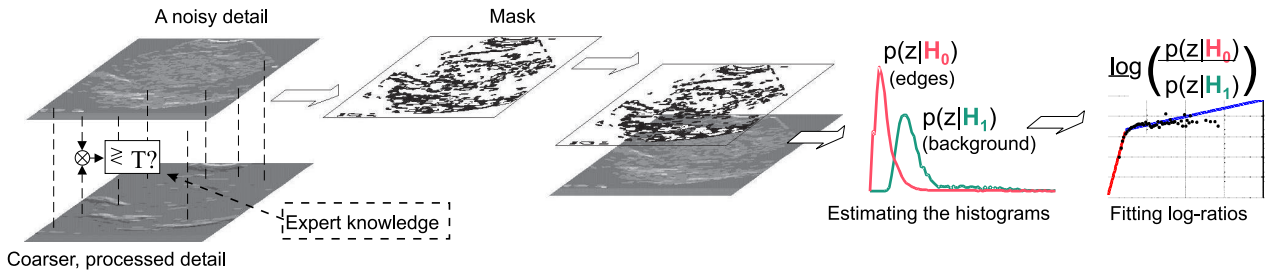


Fig. 2. Characteristic parts of the *GenLik* algorithm [12].

image at hand. A good preservation of clinically interesting features is guaranteed not only due to a local spatial adaptivity but also due to adaptivity to the preference of a medical expert-user, who can change the notion of “features of interest” by tuning a single parameter.

The *GenLik* method uses a non-decimated wavelet transform and shrinks each wavelet coefficient according to the probability that it presents a signal (or a feature) of interest, given the observed coefficient value and given a local spatial activity indicator (LSAI) calculated from the surrounding coefficients. We shall suppress the indices that denote the scale and the orientation of a wavelet subband. Let y_k and w_k respectively denote the noise-free and the observed wavelet coefficient at position k and let z_k denote LSAI at the same position. Further on, let X_k denote a binary random variable being a “significance label” for w_k . The event $X_k = 1$ reads: “ w_k represents a signal of interest” (hypothesis H_1) and the event $X_k = 0$ denotes the opposite (hypothesis H_0). Our denoiser is then

$$\hat{y}_k = P(X_k = 1|w_k, z_k)w_k = \frac{r\xi_k\eta_k}{1 + r\xi_k\eta_k}w_k, \quad (4)$$

where $r = P(X_k = 1)/P(X_k = 0)$ is the *prior ratio* and ξ_k, η_k the *likelihood ratios*, $\xi_k = p_{W_k|X_k}(w|1)/p_{W_k|X_k}(w|0)$ and $\eta_k = p_{Z_k|X_k}(z|1)/p_{Z_k|X_k}(z|0)$, which are estimated empirically from the input image.

The characteristic parts of this method are in Fig. 2: in a first stage, interscale products are compared against a threshold in order to locate the significant (“edge”) coefficients. Optionally, expert knowledge may be used to tune the threshold defining the notion of a significant feature. This preliminary classification yields a binary *mask* \hat{x} , where $x_k = 1$ indicates an edge at position k and $x_k = 0$ indicates no edge. The mask is in the next step used for the empirical estimation of the conditional probability density functions. As Fig. 2 pictorially shows, the likelihood ratios ξ_k, η_k are finally subjected to a piece-wise linear fitting in a logarithmic representation. The prior ratio is estimated as $\hat{r} = \sum_{k=1}^N \hat{x}_k / (N - \sum_{k=1}^N \hat{x}_k)$, where N is the number of coefficients in a given subband.

For a detailed analysis of this method we refer to [12] and its practical implementation is available for download at <http://telin.UGent.be/~sanja>.

D.2 Visual enhancement by speckle filtering

Two main reasons for noise suppression in images are: facilitating the subsequent (semi-)automatic processing

(next Section) and visual enhancement. Visual enhancement of ultrasound images by wavelet filtering methods has been illustrated e.g., in [7, 10]. In [12], visual results also demonstrate a *gradual* speckle suppression controlled e.g., by a medical expert-user. Fig. 3 demonstrates the effect of speckle filtering on an ultrasound brain image. The original image (Fig. 3 - left) shows a bleeding in the brain (which occurs in severe cases of white matter damage) surrounded by speckle noise. After despeckling (Fig. 3 - right) the bleeding is accentuated much better in the image.

III. ULTRASOUND IMAGE FILTERING IN THE CLINICAL STUDIES OF LEUKOMALACIA

A brain disease called *Periventricular Leukomalacia*, also called *White Matter Damage* occurs frequently on premature neonates. Due to its non-invasive nature and easily portable devices, ultrasound imaging is the main imaging modality that is nowadays used for the diagnostics and clinical studies of this brain disease. Since the quantitative analysis of medical ultrasound images is difficult and not well studied yet, physicians depend strongly on the visual interpretation of the images.

Our contacts with the clinicians in the field reveal the need for developing *semi-automatic segmentation* methods. Recent research has produced a few such semi-automatic segmentation methods, but these take little account of speckle noise. Here we show that using the right denoising approach as a preprocessing step improves significantly the segmentation performance, both in terms of accuracy and reproducibility. We make a performance comparison between the existing segmentation methods as well as the extensive evaluation of using the proposed preprocessing step. In our evaluations we incorporate *expert knowledge*, i.e., manual flare segmentations by physicians. We show that in combination with the proposed preprocessing step our novel integrated semi-automatic segmen-



Fig. 3. Left: the original image with a big bright white bleeding, surrounded by speckle noise. Right: the image denoised with the *GenLik* algorithm.

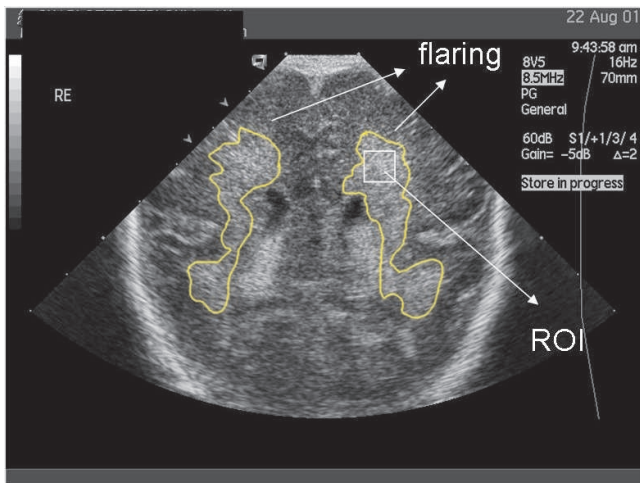


Fig. 4. Brain affected with WMD, delineated white flares. A square region of interest for texture examination is also shown.

tation method yields results that are similar to manual delineations by experts.

A. Ultrasound imaging of Periventricular Leukomalacia

A recent increase in survival rate of preterm infants has led to an increasing incidence of neurological sequelae in such infants [53]. Periventricular Leukomalacia (PVL) is characterized by deep white matter lesions adjacent to the lateral ventricles, Fig. 4. With a prevalence of 5-15% among infants born before 32 weeks of gestation, PVL is one of the best predictors of cerebral palsy in surviving preterm infants [54]. PVL is related to as well motoric dysfunction as well as visual disturbance, somatosensory disorders and cognitive deficits [55]. Thus, it is important to try and detect the pathology as early as possible. Cranial ultrasonography is frequently used for the diagnosis of PVL during the early neonatal period. Although ultrasonography is useful and non-invasive it takes a few weeks or more before the flaring becomes visible [56]. In current practice, most experts depend solely on the visual inspection of the images for the diagnosis of PVL [57]. In order to objectively support this diagnosis there is a clear demand for (semi)automated algorithms to delineate the affected regions. The main idea is to extract, in a *reproducible manner*, the contours of the disease-affected regions, which would assist doctors in following the history and the development of the disease over time.

B. Flare Segmentation

Only a few segmentation techniques were developed so far for the segmentation of the white flaring. The approach of [58] is based on active contours and uses the *Gradient Vector Flow* method of [59] combined with a single-resolution despeckling method called *GATE*. Another flare segmentation method [60] is based on *mathematical morphology*, and comprises two steps: a background reduction using a texture-feature threshold in different regions of interest (see Fig. 4), followed by a *closing* (to “fill speckle holes”) and by a *morphological gradient* (to detect the contour). Both of the above described segmentation techniques demand some form of user-interactivity by choosing the initialization points in case of the snakes or the bound-

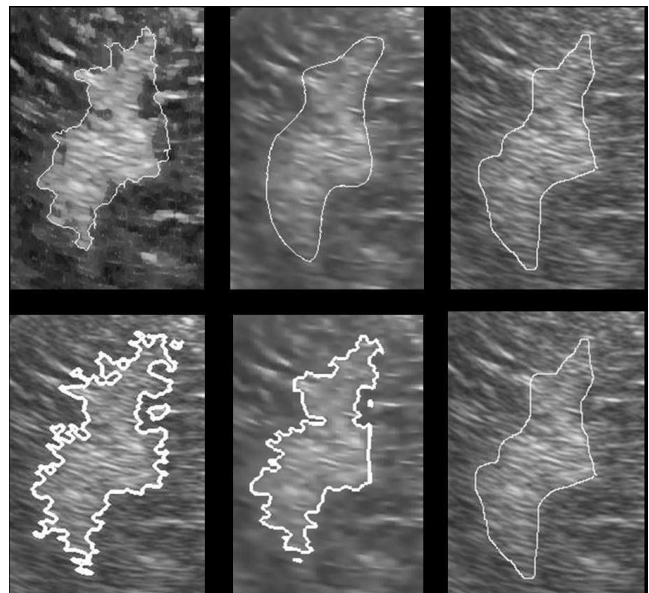


Fig. 5. Top left: snake + GATE, Top middle: snake + Genlik, Top right: manual expert delineation. Bottom left: morphology, Bottom middle: morphology + postprocessing + Genlik, Bottom right: manual expert delineation.

ing box in which the background reduction is performed in the case of the morphological technique.

Although both techniques are rather fast they still lack some stability due to the presence of speckle noise. The snake algorithm can get stuck on isolated, bright spots even if the parameters are well tuned, as can the morphological technique where little islands can occur after gradient operations. These artefact are clearly visible in the left hand images of Fig. 5. An improved morphological approach is recently developed in [61], which includes a morphological postprocessing called “opening by reconstruction”. The result of this approach can be seen in the lower part of Fig. 5.

C. Despeckling and Segmentation Accuracy

We wish to investigate how denoising affects segmentation accuracy compared to an expert-defined ground truth. For our experiments, we selected eight images in which the affected tissue (flaring) was clearly visible and asked a medical expert to manually segment the images. These manual delineations made by the medical expert are in the following used as ground truth segments.

We segmented all the tested images using the snake-technique and the improved morphological technique described above. For both approaches we made two sets of experiments: without preprocessing and with the pre-filtering using the *Genlik* algorithm from Section II-D. The parameter settings used for the morphology based technique are: a plexus threshold value of 0.9, a dilation radius of 4, an erosion radius of 3 and a preprocessing radius of 2. The parameter settings used for the active contours were $\delta = 0.2$, $\mu = 0.1$, $\alpha = 0.05$, $\beta = 0$, $\gamma = 1$ and $\kappa = 0.05$ using 80 iterations to compute the Gradient Vector Flow and 40 to iterate the snake. As threshold for the denoising technique we selected the T parameter in the interval $[0, 2]$ and used a wavelet decomposition up to scale $J = 3$

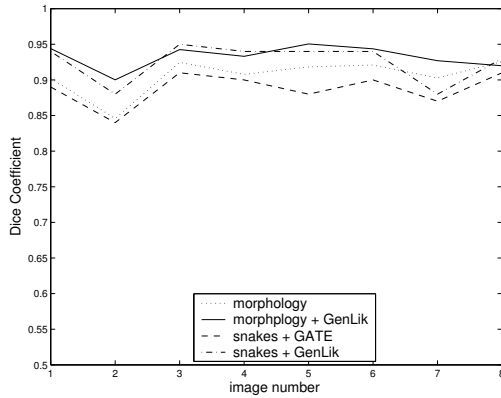


Fig. 6. Dice-coefficients for both techniques without and with the Genlik denoising.

and a window size of 5×5 . As a comparison measure between the segmentations the Dice-coefficient was used. Given two segmentation A and B , the Dice-coefficient DC is calculated as

$$DC = \frac{2\|A \cap B\|}{\|A\| + \|B\|} \quad (5)$$

where $\|A\|$ stands for the cardinality, pixel surface, of A and $A \cap B$ is the intersection of A and B . The closer the Dice-coefficient approaches 1, the more the segmentations are similar, i.e., the better they overlap.

Fig. 6 shows the Dice-coefficients for both techniques and for the eight test images, segmented without and with the tested wavelet denoising technique. The images of Fig. 5 give a visual idea of how the segmentations look like after denoising compared to the expert delineations. Both the Dice-coefficients and the visual appearance demonstrate that the use of wavelet despeckling improves the segmentation accuracy measured with respect to manual delineations by a medical expert.

D. Despeckling and Segmentation Reproducibility

Next we study the effect of wavelet denoising on the segmentation stability or *reproducibility* of its results. Since in our evaluations the improved morphological segmentation outperformed the one on active contours, we focused on the morphological technique for our next experiment. We constructed two sets of test images, which are actually the same eight images as used above, without and with denoising. Out of both test-sets, we let the computer pick an image randomly which was presented to the medical expert to segment. This continued until each of the 16 images was picked and segmented 3 times. We did this in order to scramble the images and prevent the user of using prior information if asked to segment the same image multiple times. After this segmentation part, the *Overlap Ratio* (OR) of each group of three segmentations was calculated, again using the Dice-coefficient. The results are shown in Table I. These results are in favor of wavelet denoising: for seven out of eight images the reproducibility improves due to pre-filtering with the analyzed wavelet based method.

E. Conclusions on Despeckling for Flare Segmentation

A mini-study on ultrasound brain image segmentation that is presented in this Section undoubtedly demonstrates

	OR (%) no denoising	OR (%) Genlik
image 1	92.60	93.60
image 2	92.26	92.30
image 3	90.34	95.35
image 4	89.80	91.67
image 5	91.32	93.56
image 6	95.75	95.79
image 7	92.09	94.34
image 8	98.80	91.67

TABLE I
OVERLAP RATIOS FOR THE TWO TEST SET WITHOUT AND WITH
GENLIK DENOISING

the usefulness of wavelet domain noise reduction in this application. As can be seen from Fig. 5, after denoising the segmented contours are less fragmented, and are closer to the manual segmentations by medical experts. Our experiments demonstrated that the reproducibility of the segmentation also improves after wavelet domain denoising. This proves that indeed there is a real meaning to the noise reduction as a pre-processing step in this application.

Compared to the analyzed single-resolution GATE despeckling method for ultrasound images, the tested wavelet filter proved advantageous, both visually (Fig. 5) and in terms of objective performance measures (Fig. 6). It is worth mentioning that the morphological segmentation technique of [61] analyzed here with the wavelet domain *Genlik* denoiser is nowadays already tested in clinical practice at the neonatology department of the *Sofia Children's Hospital* Rotterdam, The Netherlands.

IV. DENOISING MRI IMAGES

In magnetic resonance imaging the practical limits of the acquisition time impose a trade-off between SNR and image resolution (see, e.g., [62–64]). The acquisition time is limited in practice due to the patient comfort and physical limitations (especially in dynamic applications, such as cardiac imaging and functional MRI [65]). Post-processing noise reduction is therefore often seen as the only means of achieving a desired MRI image quality. Wavelet based denoising methods for MRI and *fMRI* images include [4, 6, 11, 12, 17]. The first ones were based on simple soft-thresholding [17], and the more recent ones often incorporate the coefficient propagation across scales in the form of *multiscale products* [4, 11, 26] and combining these multiscale products with the spatial context [12].

A. Noise in MRI

The main source of noise in MRI images is the thermal noise in the patient [66]. The MRI image is commonly reconstructed by computing the inverse discrete Fourier transform of the raw data [63]. The signal component of the measurements is present in both real and imaginary channels; each of the two orthogonal channels is affected by additive white Gaussian noise. The noise in the reconstructed complex-valued data is thus complex white Gaussian noise.

Most commonly, the *magnitude* of the reconstructed MRI image is used for visual inspection and for automatic computer analysis. Since the magnitude of the MRI signal is the square root of the sum of the squares of two

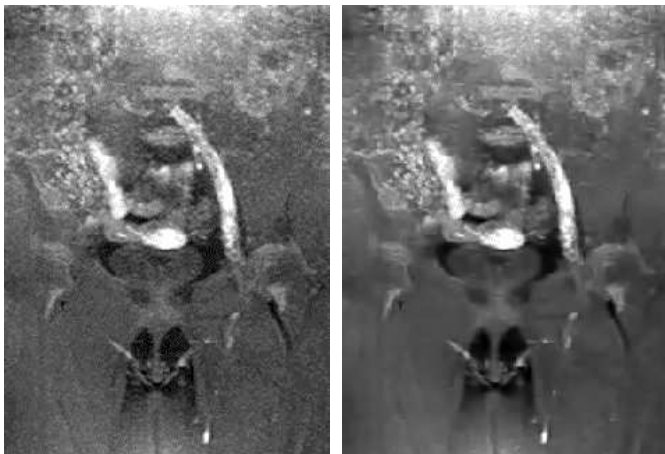


Fig. 7. Left: an original MRI image magnitude. Right: the result of a wavelet denoising method for Rician noise from Section IV-B.

independent Gaussian variables, it follows a Rician distribution. In low intensity (dark) regions of the magnitude image, the Rician distribution tends to a Rayleigh distribution [67] and in high intensity (bright) regions it tends to a Gaussian distribution. A practical consequence is a reduced image contrast: noise increases the mean value of pixel intensities in dark image regions.

Due to the signal-dependent mean of the Rician noise, both the wavelet and the scaling coefficients of a noisy MRI image are *biased* estimates of their noise-free counterparts. In [65] it was shown that one can efficiently overcome this problem by filtering the *square* of the MRI magnitude image in the wavelet domain. In the squared magnitude image, data are non-central chi-square distributed, and the wavelet coefficients are no longer biased estimates of their noise-free counterparts. The bias still remains in the scaling coefficients, but is not signal-dependent and it can be easily removed: at the resolution scale 2^j , from each scaling coefficient $2^{j+1}\sigma_c$ should be subtracted, where σ_c^2 is the underlying complex Gaussian noise variance. This value is typically estimated from the noisy image: MRI images include an empty region of air outside the patient; in the squared magnitude image, the average pixel value in those empty (border) regions is $2\sigma_c^2$.

B. Adapted GenLik method for Rician noise

According to the explanation given above, the *GenLik* algorithm from Section II-D should be adapted for the suppression of Rician noise in MRI image magnitude as follows:

- Compute the square of the MRI magnitude image;
- Compute the non-decimated wavelet transform with L decomposition levels (in practice, we used $L=4$);
- Estimate the wavelet coefficients as described in Section II-D;
- Subtract $2^{L+1}\sigma_c$ from the scaling coefficients;
- Apply the inverse wavelet transform;
- Compute the square root of the image.

Fig. 7 illustrates the application of this method to one real MRI image magnitude, and in the next Section, we study its application to *fMRI* images.

V. DENOISING OF FUNCTIONAL MRI (*fMRI*) TIME SERIES

This section analyzes a number of wavelet-based denoising schemes for *fMRI* time series data experimentally.

A. Analysis of *fMRI* data

An *fMRI* data set is a sequence of three-dimensional (3D) MR images, recorded while the person in the scanner performs a specific task. Most *fMRI* analysis methods are based on the general linear model (GLM), which models the total brain response as the superposition of all individual stimulus responses [68]. In the GLM, the response to each stimulus is modelled as the output of a linear, time-invariant (LTI) system. Such a system is characterised by its impulse response, which, in the case of *fMRI* analysis, is denoted as the haemodynamic response function (HRF). The response signal to each type of stimulus is given by the convolution of the time pattern in which these stimuli occur, and the HRF corresponding with that type of stimulus. Such a response signal is called an *effect of interest*.

The analysis of *fMRI* data in the GLM is done via the following formula:

$$\mathbf{Y}_{[T \times N]} = \mathbf{X}_{[T \times M]}\boldsymbol{\beta}_{[M \times N]} + \mathbf{e}_{[T \times N]}. \quad (6)$$

Here, \mathbf{Y} is the *fMRI* data of T time points and N voxels (volume elements), \mathbf{X} is the *design matrix*, whose row vectors are the modelled effects. These may be effects of interests (such as modelled response) and effects of no interest (such as movement-related artefacts or cardiac signals). The matrix $\boldsymbol{\beta}$ contains the weight of each effect in each voxel. The residual signal (the part of the signal not modelled in \mathbf{X}) ends up in the matrix \mathbf{e} . The brain regions that have a significant contribution to the task are selected via hypothesis testing, i.e., regions whose voxel locations have significantly high values in the row of $\boldsymbol{\beta}$ that corresponds to the task, are considered significant.

Hypothesis testing may be done with either parametric [69] or nonparametric [70] statistical methods. The latter have the advantage that they do not require any assumptions about the distributions of the noise. The main advantage of the former is that they are computationally less demanding, while the methods are quite robust to deviations from the assumed noise distribution (which is usually Gaussian). Most hypothesis tests compare the magnitude of the effects of interest with a threshold based on the distribution of the noise in the data. After the transformation described in (6), a good estimate for the noise (provided the predictable effects are modelled as well as possible by \mathbf{X}) is given by \mathbf{e} . Smaller values in \mathbf{e} lead to lower statistic thresholds, and therefore better detection. Good denoising methods lower the noise amplitudes, but keep the signal intact.

B. Tested wavelet denoising methods for *fMRI*

The most common preprocessing step in *fMRI* data analysis is to apply a Gaussian smoothing, i.e., by filtering the images with a lowpass Gaussian kernel. Gaussian smoothing decreases the noise amplitude, but it also changes the shape of the signal. Specifically, fine (high-frequency) features in the images are obscured by smoothing. We examine the performance of wavelet-based denois-

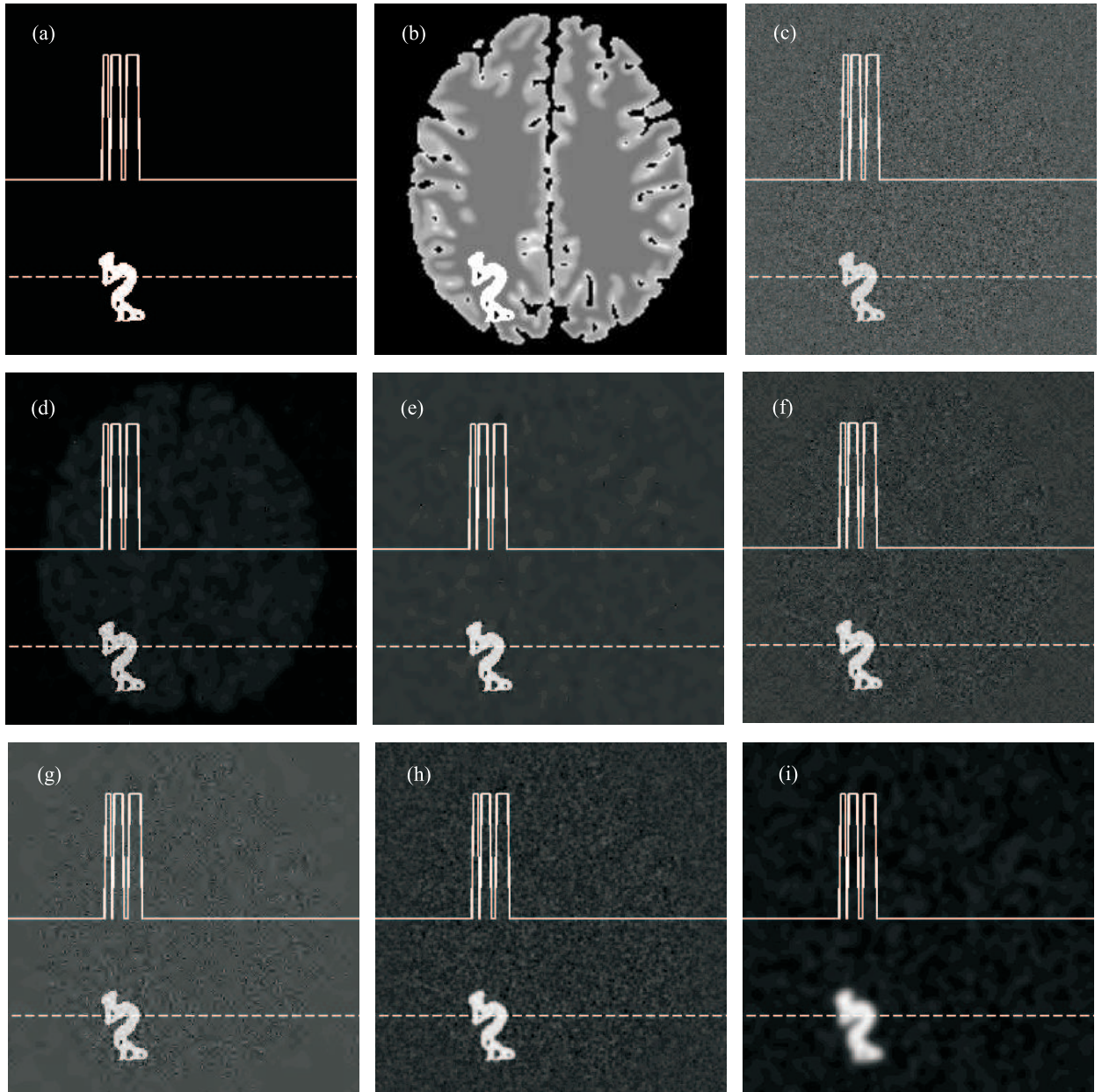


Fig. 8. **Top row** - images used in the experiment: (a) the active region with a line profile (solid line) taken from the image (dotted line), (b) the noise-free template image from the *BrainWeb* simulator with the active region shown in white, (c) the BOLD image made by subtracting two noisy images with $\text{SNR} = 18$ dB. **Middle and bottom rows** - denoising results: (d) *GenLik* for Rician noise ($\text{SNR}=4.5$ dB), (e) basic *GenLik* ($\text{SNR}=7.9$ dB), (f) *InvShrink* ($\text{SNR}=3.0$ dB), (g) the *MinMaxThresh* ($\text{SNR}=3.6$ dB), and (h) *Gaussian smoothing* with $\text{FWHM} = 1$ pixel ($\text{SNR}=3.3$ dB) and (i) $\text{FWHM} = 4 \times 4$ pixels ($\text{SNR}=3.2$ dB).

ing methods in the setting of *fMRI* analysis, by comparing them with the traditional Gaussian smoothing.

The *WaveLab* package [71] contains some of the most well-known wavelet-based denoising methods in use today. They have been demonstrated in the *fMRI* setting and compared to Gaussian smoothing [72]. In that paper, tests are done on synthetic BOLD images, constructed by subtracting pairs of MR images which both contain synthetic Rician noise [?, 73, 74]. The activation time signal is a block signal. Another test is done on a real data set, also with a block activation pattern.

We use the WaveLab-based methods *InvShrink* and

MinMaxThresh, presented in [72]. We also use the *GenLik* denoising method of [12], both in its basic form, as described in Section II-D, and with the adaptation for Rician noise, which consists in applying the same method to the squared image and compensating for the bias in the scaling coefficients (see Sec. IV-B). Finally, we use two degrees of Gaussian smoothing: FWHM ($\text{FWHM} = \text{full width at half maximum} = 4 \times 4 \times 4 \text{ mm}^3$ (or one pixel) and $\text{FWHM} = 12 \times 12 \times 12 \text{ mm}^3$ (or 4×4 pixels).

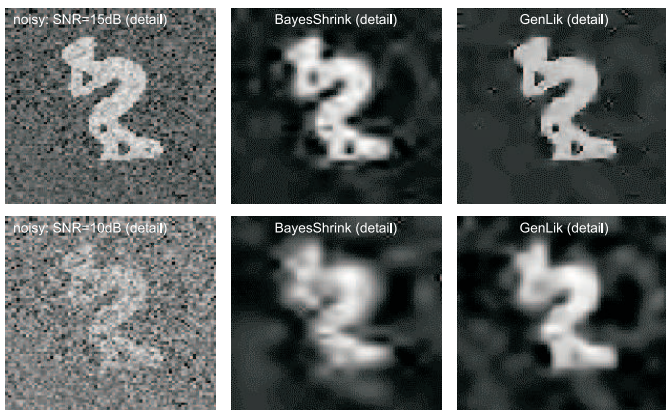


Fig. 9. Denoising artificial bold images (left) using a soft-thresholding method *BayesShrink* of [23] (middle) and using the *Genlik* method (right).

C. Artificial BOLD images

The blood oxygenation level dependent (BOLD) contrast is computed as the difference between two MR images. These two MR images have Rician distributed grey values. The distribution of the difference of two Rician sets is symmetric and near-Gaussian [72]. We used a simulated MR image from the BrainWeb simulator [75] without noise. Rician distributed noise with a known SNR was added to 2 copies of the image, of which one contained an active spot (see Fig. 8a-b), where the signal was increased by 5% of the maximum grey value. After adding the noise, the images had an SNR of 18 dB. The BOLD image made by subtracting the images (see Fig. 8c) had an SNR of -0.1 dB. After applying the preprocessing steps described above, the SNR was measured again.

Figure 8(d-i) shows the results for the tested methods. The denoised BOLD image is presented and overlaid with a cross-section of the image (fixed line) at a location inside the active region (indicated by the dotted line). All the tested wavelet methods outperform the Gaussian smoothing (Fig. 8i) and the basic *Genlik* method from Section II-D achieves the best result (Fig. 8d). Fig. 9 compares the performance of the *Genlik* method and the Bayesian wavelet thresholding method *BayesShrink* of [23], which uses a uniform threshold per subband that is optimized in terms of the mean-squared error. This figure illustrates that wavelet based methods can preserve the shape of the activated region remarkably well even in cases of severe noise. In this respect, it is however advantageous to use a sophisticated locally adaptive wavelet method instead of a global thresholding with a uniform threshold per subband.

D. Time series of MR images

A sequence of real MR images was recorded without presenting stimuli. This *null experiment* is assumed to contain only noise [76]. The images are gradient echo EPI images collected with a Bruker Medspec 3.0T system at the Wolfson Brain Imaging Centre, Cambridge. The images are $64 \times 64 \times 21$ voxels, with voxel size $3.9 \times 3.9 \times 5$ mm³. Realignment and spin excitation history correction were done with BAMB software [77], to remove as many artefacts as possible from the data. Activation with a spatial

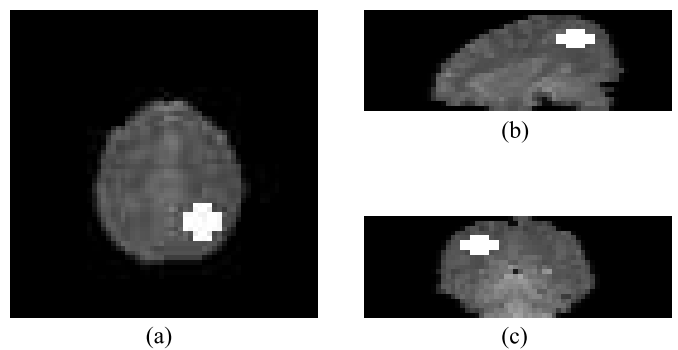


Fig. 10. The shape of the active region: (a) transverse view, (b) sagittal view and (c) coronal view.

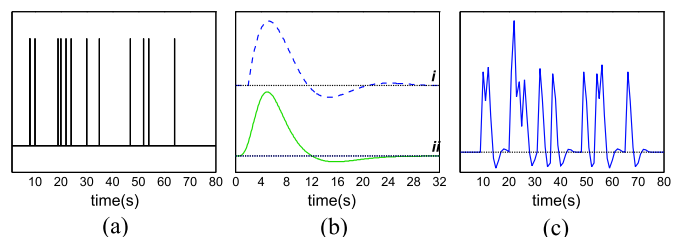


Fig. 11. (a) The stimulus sequence. (b) The damped harmonic oscillator HRF that was used to model the activation (*i*) and the gamma density HRF (*ii*) that was used to estimate the GLM. (c) The modelled response.

pattern as shown in fig. 10 was added to the data. The time pattern of the activation was made by convolving a randomised stimulus sequence (see fig. 11a) with a haemodynamic response function (HRF). The HRF describes the changes in regional blood flow (and therefore also in the *fMRI* time signal) following a very short stimulus. We model the HRF as the impulse response function of a 4-element windkessel [78, 79], which is a damped harmonic oscillator (see fig. 11b). The parameters of the function were chosen so as to resemble some more common HRFs, such as the one composed of two gamma density functions (see fig. 11b). Figure 11c shows the time signal.

After adding the activation, copies of the MRI time series were processed with the different methods. Each denoised version of the time series was then analysed with the *SPM* software [69]. The matrix \mathbf{X} [see 6] consisted of an ‘expected’ response and a constant signal (to represent the time series mean). To make the experiment more realistic, the estimated response was not completely the same as the ‘real’ response: the response in \mathbf{X} was constructed by convolving the stimuli with the gamma density HRF.

After estimating the GLM, the variance ratio was computed in each voxel. The variance ratio is the amount of variance explained by the model, divided by the amount of variance in the residual. Active regions were found by performing an *F*-test on the voxels in the parametric maps. Activated regions (after thresholding the maps at $p=0.001$) are shown in Fig. 12.

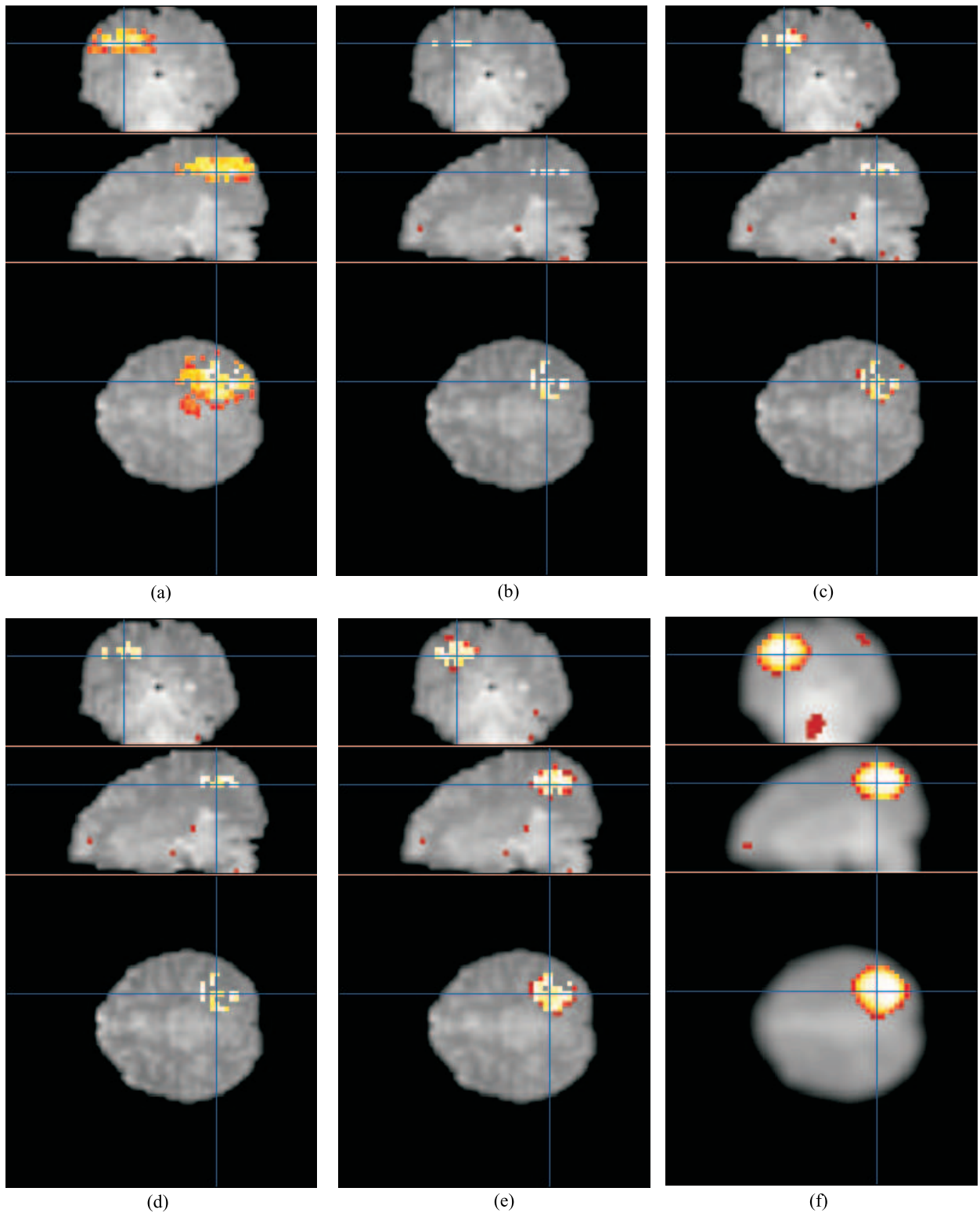


Fig. 12. Statistical maps of the time series after different preprocessing steps: (a) *Genlik* method adapted for Rician noise (b) basic *Genlik*, (c) *InvShrink*, (d) *MinMaxThresh*, and (e) *Gaussian smoothing* with $\text{FWHM} = 4 \times 4 \times 4 \text{ mm}^3$ and (f) $\text{FWHM} = 12 \times 12 \times 12 \text{ mm}^3$.

E. Discussion on fMRI denoising

The results on the tested real MRI sequence, presented above show that despite the various models that exist for fMRI noise (both spatial and temporal), the real case is usually still hard to analyse. When the *Genlik* method is applied to the squared image (Rician noise version), a large area is detected around the original spot, that is quite different in shape than the original active region. This is due to the local variance component used to predict the local distributions of noise and signal. EPI images have low contrast, and the (erratic) shapes found in the brain bias the classification. The basic *Genlik* method (applied to the original and not squared image) is much more conservative, and detects only a portion of the original region. The number of false positives, however, is also very small.

The *WaveLab*-methods from [72] perform similarly to the latter one. Large portions of the original spot are missing, but there are few false positives.

Gaussian smoothing with a kernel of $4 \times 4 \times 4 \text{ mm}^3$ (which is a bit smaller than the voxel size) gives quite good results. The shape of the original activation is well detected. The number of false positives is larger than those of the Gaussian noise and wavelet-based methods, but the number of false positives is lower. Gaussian smoothing with a large smoothing kernel ($12 \times 12 \times 12 \text{ mm}^3$) gives the notorious smoothing-related deformations: heavily deformed detected regions with many false positives, and large detected areas at other locations.

A possible explanation for the difference between the results of the simulations and this real data example is that the *Genlik* method is tuned to too fine resolution as compared to the fMRI sequence we experimented with. Also, the performance of the *WaveLab* may be affected by violations of the assumptions about the noise distribution (Gaussian smoothing does not use such assumptions, while *WaveLab* methods do). Another explanation may be the presence of disturbing factors in the data, which need to be removed before a proper analysis can be done. One important thing to consider is that when the assumptions used by the denoising algorithms do not hold, it is not likely that statistical tests based on these assumptions can be applied correctly. In the case of statistical mapping, the nonparametric approach [70,80] may be a good alternative.

VI. CONCLUSION

In this paper some practical applications of wavelet domain denoising in ultrasound and in MRI imaging were demonstrated. The presented results demonstrate the usefulness of wavelet denoising for visual enhancement of images as well as for improving some further automatic processing like the segmentation of ultrasound images.

In case of the ultrasound imaging, the interactive noise reduction scheme, taking into account prior information as well as local regional statistics lead to a more naturally ultrasound image, in which anatomical features were better kept intact. This preprocessing step undeniably lead to a more stable, reproducible segmentation than was known up to now. We obtained contours that are more similar to the delineations of the medical experts and were able to prove that as well visually as mathematically. In current medical practice, this means that the experts, once they classified the image as being malignant, by setting a simple

threshold can visualize the pathology.

In case of fMRI, wavelet based denoising methods have shown to be effective in terms of improving SNR as well as preserving the shape of the activated region. It has to be mentioned, however, that the results on real fMRI data, where denoising was combined with the statistical parametric mapping, were somewhat disappointing compared to the purely simulated cases. There is still a delicate tradeoff between sensitivity (the ability to detect the target region) and specificity (the ability to not detect non-target regions) in fMRI analysis. New wavelet-based methods are currently in development, and will hopefully contribute to finding the optimal balance between detection power and control of false positives.

REFERENCES

- [1] I. Daubechies, *Ten Lectures on Wavelets*, Philadelphia: SIAM, 1992.
- [2] S. Mallat, *A wavelet tour of signal processing*. Academic Press, London, 1998.
- [3] M. Vetterli and J. Kovačević, *Wavelets and Subband Coding*. Prentice-Hall, 1995.
- [4] Y. Xu, J. B. Weaver, D. M. Healy, and J. Lu, "Wavelet transform domain filters: a spatially selective noise filtration technique," *IEEE Trans. Image Proc.*, vol. 3, no. 6, pp. 747–758, Nov. 1994.
- [5] M. Unser and A. Aldroubi, "A review of wavelets in biomedical applications," *Proc. of the IEEE*, vol. 84, no. 4, pp. 626–634, Apr. 1996.
- [6] M. Hilton, T. Ogden, D. Hattery, G. Eden, and B. Jawerth, "Wavelet processing of functional MRI data," in *Wavelets in Biology and Medicine*, A. Aldroubi and M. Unser, Eds. CRC Press, 1996.
- [7] F. Sattar, L. Floreby, G. Salomonsson, and B. Lövfström, "Image enhancement based on a nonlinear multiscale method," *IEEE Trans. Image Proc.*, vol. 6, no. 6, pp. 888–895, 1997.
- [8] R. Q. Quiroga and H. Garcia, "Single-trial event-related potentials with wavelet denoising," *Clinical Neurophysiology*, vol. 114, no. 2, pp. 376–390, 2003.
- [9] E. T. Bullmore, C. Long, J. Suckling, J. Fadili, G. Calvert, F. Zelaya, T. A. Carpenter, and M. Brammer, "Colored noise and computational inference in neurophysiological (fMRI) time series analysis: Resampling methods in time and wavelet domains," *Human Brain Mapping*, vol. 12, pp. 61–78, 2001.
- [10] A. Achim, A. Bezerianos, and P. Tsakalides, "Novel Bayesian multiscale method for speckle removal in medical ultrasound images," *IEEE Trans. Medical Imaging*, vol. 20, no. 8, pp. 772–783, Aug. 2001.
- [11] P. Bao and L. Zhang, "Noise reduction for magnetic resonance images via adaptive multiscale products thresholding," *IEEE Trans. Med. Imaging*, vol. 22, no. 9, pp. 1089–1099, 2003.
- [12] A. Pižurica, W. Philips, I. Lemahieu, and M. Acheroy, "A versatile wavelet domain noise filtration technique for medical imaging," *IEEE Trans. Medical Imaging*, vol. 22, no. 3, pp. 323–331, Mar. 2003.
- [13] D. L. Donoho, "De-noising by soft-thresholding," *IEEE Trans. Inform. Theory*, vol. 41, pp. 613–627, May 1995.
- [14] I. M. Johnstone and B. W. Silverman, "Wavelet threshold estimators for data with correlated noise," *Journal of the Royal Statistical Society*, vol. 59, no. 2, pp. 319–351, 1997.
- [15] F. Abramovich and Y. Benjamini, "Adaptive thresholding of wavelet coefficients," *Computational Statistics and Data Analysis*, vol. 22, pp. 351–361, 1996.
- [16] R. R. Coifman and D. L. Donoho, "Translation-invariant denoising," in *Wavelet and Statistics*, ser. Lecture Notes in Statistics, A. Antoniadis and G. Oppenheim, Eds. Springer, 1995, pp. 125–150.
- [17] D. H. J. Weaver, Y. Xu and J. Driscoll, "Filtering mr images in the wavelet transform domain," *Magn. Reson. Med*, vol. 21, no. 3, pp. 288–295, 1991.
- [18] H. A. Chipman, E. D. Kolaczyk, and R. E. McCulloch, "Adaptive Bayesian wavelet shrinkage," *J. of the Amer. Statist. Assoc.*, vol. 92, pp. 1413–1421, 1997.
- [19] M. Clyde, G. Parmigiani, and B. Vidakovic, "Multiple shrinkage

- and subset selection in wavelets," *Biometrika*, vol. 85, no. 2, pp. 391–401, 1998.
- [20] B. Vidakovic, "Wavelet-based nonparametric Bayes methods," in *Practical Nonparametric and Semiparametric Bayesian Statistics*, ser. Lecture Notes in Statistics, D. D. Dey, P. Müller, and D. Sinha, Eds., vol. 133. Springer Verlag, New York, 1998, pp. 133–155.
- [21] F. Abramovich, T. Sapatinas, and B. W. Silverman, "Wavelet thresholding via a Bayesian approach," *J. of the Royal Statist. Society B*, vol. 60, pp. 725–749, 1998.
- [22] S. G. Chang, B. Yu, and M. Vetterli, "Spatially adaptive wavelet thresholding with context modeling for image denoising," in *Proc. IEEE Internat. Conf. on Image Proc.*, Chicago, IL, Oct. 1998.
- [23] —, "Adaptive wavelet thresholding for image denoising and compression," *IEEE Trans. Image Proc.*, vol. 9, no. 9, pp. 1532–1546, Sept. 2000.
- [24] L. Şendur and I. W. Selesnick, "Bivariate shrinkage functions for wavelet -based denoising exploiting interscale dependency," *IEEE Trans. Signal Proc.*, vol. 50, no. 11, pp. 2744–2756, Nov. 2002.
- [25] —, "Bivariate shrinkage with local variance estimation," *IEEE Signal Proc. Letters*, vol. 9, no. 12, pp. 438–441, Dec. 2002.
- [26] F. D. Murtagh and J. L. Starck, "Bayes factors for edge detection from wavelet product spaces authors," *Optical Engineering*, vol. 42, pp. 1375–1382, May 2003.
- [27] M. A. T. Figueiredo and R. D. Nowak, "An EM algorithm for wavelet-based image restoration," *IEEE Transactions on Image Processing*, vol. 12, no. 7, 2003.
- [28] P. Moulin and J. Liu, "Analysis of multiresolution image denoising schemes using generalized Gaussian and complexity priors," *IEEE Trans. Inform. Theory*, vol. 45, pp. 909–919, Apr. 1999.
- [29] M. K. Mihçak, I. Kozintsev, K. Ramchandran, and P. Moulin, "Low-complexity image denoising based on statistical modeling of wavelet coefficients," *IEEE Signal Proc. Lett.*, vol. 6, no. 12, pp. 300–303, Dec. 1999.
- [30] X. Li and M. Orchard, "Spatially adaptive denoising under over-complete expansion," in *Proc. IEEE Internat. Conf. on Image Proc.*, Vancouver, Canada, Sept. 2000.
- [31] J. Portilla, V. Strela, M. J. Wainwright, and E. P. Simoncelli, "Image denoising using Gaussian scale mixtures in the wavelet domain," *IEEE Trans. Image Proc.*, vol. 12, no. 11, pp. 1338–1351, Nov. 2003.
- [32] M. Malfait and D. Roose, "Wavelet-based image denoising using a Markov random field a priori model," *IEEE Trans. Image processing*, vol. 6, no. 4, pp. 549–565, Apr. 1997.
- [33] M. Jansen and A. Bultheel, "Empirical Bayes approach to improve wavelet thresholding for image noise reduction," *J. Amer. Stat. Assoc.*, vol. 96, no. 454, pp. 629–639, 2001.
- [34] A. Pižurica, W. Philips, I. Lemahieu, and M. Acheroy, "A joint inter- and intrascale statistical model for wavelet based Bayesian image denoising," *IEEE Trans. Image Proc.*, vol. 11, no. 5, pp. 545–557, May 2002.
- [35] M. S. Crouse, R. D. Nowak, and R. G. Baraniuk, "Wavelet-based statistical signal processing using hidden Markov models," *IEEE Trans. Signal Proc.*, vol. 46, no. 4, pp. 886–902, 1998.
- [36] J. K. Romberg, H. Choi, and R. G. Baraniuk, "Bayesian tree structured image modeling using wavelet-domain hidden Markov models," in *Proc. SPIE Technical Conf. on Mathematical Modeling, Bayesian Estimation, and Inverse Problems*, Denver, CO, July 1999.
- [37] G. Fan and X. G. Xia, "Image denoising using local contextual hidden Markov model in the wavelet domain," *IEEE Signal Processing Letters*, vol. 8, no. 5, pp. 125–128, May 2001.
- [38] J. W. Goodman, "Some fundamental properties of speckle," *J. Opt. Soc. Am.*, vol. 66, pp. 1145–1150, 1976.
- [39] R. F. Wagner, S. W. Smith, J. M. Sandrik, and H. Lopez, "Statistics of speckle in ultrasound b-scans," *IEEE Trans. on Sonics and Ultrasonics*, vol. 30, no. 3, pp. 156–163, May 1983.
- [40] J. S. Lee, "Digital image enhancement and noise filtering by use of local statistics," *IEEE Trans. Pattern Anal. and Machine Intel.*, vol. 2, no. 2, pp. 165–168, Mar. 1980.
- [41] V. S. Frost, J. A. Stiles, K. S. Shanmugan, and J. C. Holtzman, "A model for radar images and its application to adaptive digital filtering of multiplicative noise," *IEEE Trans. Pattern Anal. and Machine Intell.*, vol. 4, no. 2, pp. 157–166, Mar. 1982.
- [42] D. T. Kuan, A. A. Sawchuk, T. C. Strand, and P. Chavel, "Adaptive noise smoothing filter for images with signal-dependent noise," *IEEE Trans. Pattern Anal. and Machine Intel.*, vol. 7, no. 2, pp. 165–177, Mar. 1985.
- [43] A. Lopes, R. Touzi, and E. Nezry, "Adaptive speckle filters and scene heterogeneity," *IEEE Transaction on Geosc. and Remote Sens.*, vol. 28, no. 6, pp. 992–1000, Nov. 1990.
- [44] T. R. Crimmins, "Geometric filter for speckle reduction," *Appl. Optics*, vol. 24, pp. 1438–1443, 1985.
- [45] L. Gagnon and A. Jouan, "Speckle filtering of SAR images - a comparative study between complex-wavelet-based and standard filters," in *Proc. SPIE, no. 3169, conference "Wavelet Applications in Signal and Image Processing V*, San Diego 1997.
- [46] J. E. Odegard, H. Guo, M. Lang, C. S. Burrus, and R. O. Wells, "Wavelet based SAR speckle reduction and image compression," in *Proc. SPIE Symposium on OE/Aerospace Sensing and Dual Use Photonics*, Orlando, Florida, April 1995.
- [47] L. Gagnon and F. D. Smaili, "Speckle noise reduction of airborne SAR images with symmetric daubechies wavelets," in *Proc. SPIE, no. 2759, conference "Signal and Data Processing of Small Targets*, Orlando 1996.
- [48] S. Foucher, G. B. Benie, and J. M. Boucher, "Multiscale MAP filtering of SAR images," *IEEE Trans. Image Proc.*, vol. 10, pp. 49–60, Jan. 2001.
- [49] G. Kossof, W. J. Garret, D. A. Carpenter, J. Jellins, and M. J. Dadd, "Principles and classification of soft tissues by gray scale echography," *Ultrasound Med. Biol.*, vol. 2, pp. 89–105, 1976.
- [50] F. G. Sommer, L. F. Joynt, B. A. Carroll, and A. Macowski, "Ultrasonic characterization of abdominal tissues via digital analysis of backscattered waveforms," *Radiology*, vol. 141, pp. 811–817, Dec. 1981.
- [51] S. Z. Li, *Markov Random Field Modeling in Computer Vision*. Springer-Verlag, 1995.
- [52] D. Middleton and R. Esposito, "Simultaneous optimum detection and estimation of signals in noise," *IEEE Trans. Inform. Theory*, vol. 14, no. 3, pp. 434–443, May 1968.
- [53] D. Davis, "Review of cerebral palsy," *Neonatal Network*, vol. 16.
- [54] N. Paneth, R. Nudelli, E. Kazam, and W. Monte, "Brain damage in the preterm infant," *Mac Keith Press, London*, 1994.
- [55] S. Fujimoto, N. Yamaguchi, H. Togari, Y. Wada, and K. Yokochi, "Cerebral palsy of cystic periventricular leukomalacia in low-birth-weight infants." *Acta Paediatr.*, vol. 83, pp. 397–401, 1994.
- [56] F. S. Pidcock, L. J. Graziani, C. Stanley, D. G. Mitchell, and D. Merton, "Neurosonographic features of periventricular echodensities associated with cerebral palsy in the preterm infant," *Journal of Pediatrics*, vol. 116, pp. 417–422, 1990.
- [57] A. Peelen and P. Govaert, *Chorioamnionitis and flaring*. Sophia Children's Hospital, Rotterdam, Holland, 2002.
- [58] G. Stippel, I. Duskunovic, W. Philips, I. Lemahieu, A. Zecic, and P. Govaert, "Segmenting flares in ultrasound images using prior statistics," *Image Processing and Communications, Vol. 7, no. 1-2, p.p. 41-54*, vol. 7, pp. 41–54, 2001.
- [59] C. Zu and J. L. Prince, "Gradient vector flow: a new external force for snakes," *Conference on computer Vision and Pattern Recognition (CVPR '97)*, pp. 66–71, 1997.
- [60] E. Vansteenkiste, G. Stippel, P. Govaert, A. Ledda, and W. Philips, "Segmenting leukomalacia using textural information and mathematical morphology," *Proceedings of STW/ProRISC, Veldhoven, The Netherlands*, pp. 441–446, 2003.
- [61] E. Vansteenkiste, A. Pižurica, A. Ledda, and W. Philips, "Improved segmentation of ultrasound brain tissue incorporating expert evaluation," in *IEEE International Conf. on Image Processing ICIP 2005 (submitted)*, Genova, Italy, Sep. 2005.
- [62] H. Gudbjartsson and S. Patz, "The Rician distribution of noisy MRI data," *Magn. Reson. Med.*, vol. 34, pp. 910–914, 1995.
- [63] A. Macovski, "Noise in MRI," *Magn. Reson. Med.*, vol. 36, pp. 494–497, 1996.
- [64] E. R. McVeigh, R. M. Henkelman, and M. J. Bronskill, "Noise and filtration in magnetic resonance imaging," *Med. Phys.*, vol. 3, pp. 604–618, 1985.
- [65] R. D. Nowak, "Wavelet-based Rician noise removal for magnetic resonance imaging," *IEEE Trans. Image Proc.*, vol. 8, pp. 1408–1419, Oct. 1999.
- [66] W. A. Edelstein, G. Glover, C. Hardy, and R. Redington, "The intrinsic signal-to-noise ratio in NMR imaging," *Magn. Reson. Med.*, vol. 3, pp. 604–618, 1986.

- [67] A. Papoulis, *Probability, random variables, and stochastic processes*. McGraw-Hill, 1984.
- [68] G. M. Boynton, S. A. Engel, G. H. Glover, and D. J. Heeger, "Linear systems analysis of functional magnetic resonance imaging in human V1," *The Journal of Neuroscience*, vol. 16, no. 13, pp. 4207–4221, July 1996.
- [69] K. J. Friston, A. P. Holmes, K. J. Worsley, J. P. Poline, C. D. Frith, and R. S. J. Frackowiak, "Statistical parametric maps in functional imaging: A general linear approach," *Human Brain Mapping*, vol. 2, pp. 189–210, 1995, <http://www.fil.ion.ucl.ac.uk/spm>.
- [70] E. T. Bullmore, M. J. Brammer, S. C. R. Williams, S. Rabe-Hesketh, N. Janot, A. David, J. Mellers, R. Howard, and P. Sham, "Statistical methods of estimation and inference for functional MR image analysis," *Magnetic Resonance in Medicine*, vol. 35, no. 2, pp. 261–277, 1996.
- [71] J. B. Buckheit and D. L. Donoho, "Wavelab and reproducible research," Dept. of statistics, Stanford University, Tech. Rep. 474, 1995, <http://www-stat.stanford.edu/~wavelab>.
- [72] A. M. Wink and J. B. T. M. Roerdink, "Denoising functional MR images: a comparison of wavelet denoising and Gaussian smoothing," *IEEE Transactions on Medical Imaging*, vol. 23, no. 3, pp. 374–387, 2004.
- [73] S. O. Rice, "Mathematical analysis of random noise III-IV," *Bell System Technical Journal*, vol. 24, no. 46-156, 1945.
- [74] J. Sijbers, A. J. den Dekker, J. V. Audekerke, M. Verhoye, and D. V. Dyck, "Estimation of the noise in magnitude MR images," *Magnetic Resonance Imaging*, vol. 16, no. 1, pp. 87–90, 1998.
- [75] R. K.-S. Kwan, A. C. Evans, and G. B. Pike, "An extensible MRI simulator for post-processing evaluation," in *Proc. Visualization in Biomedical Computing*, ser. Lecture Notes in Computer Science, vol. 1131, 1996, pp. 135–140, <http://www.bic.mni.mcgill.ca/brainweb>.
- [76] V. T. Maxim, L. S. Sendur, M. J. Fadili, J. Suckling, R. L. Gould, R. Howard, and E. T. Bullmore, "Fractional gaussian noise and functional magnetic resonance imaging," *NeuroImage*, vol. 24, 2005, in press.
- [77] E. T. Bullmore, M. J. Brammer, S. Rabe-Hesketh, V. A. Curtis, R. G. Morris, S. C. R. Williams, T. Sharma, and P. K. McGuire, "Methods for diagnosis and treatment of stimulus-correlated motion in generic brain activation studies using fMRI," *Human Brain Mapping*, vol. 7, pp. 38–48, 1999.
- [78] J. B. Mandeville, J. J. Marota, C. Ayata, G. Zaharchuk, M. A. Moskowitz, B. R. Rosen, and R. M. Weisskoff, "Evidence of a cerebrovascular postarteriole windkessel with delayed compliance," *Journal of Cerebral Blood Flow and Metabolism*, vol. 19, no. 6, pp. 679–689, 1999.
- [79] N. Stergiopoulos, B. E. Westerhof, and N. Westerhof, "Total arterial inertance as the fourth element of the windkessel model," *American Journal of Physiology*, vol. 276, no. 1, pp. 81–88, 1999.
- [80] T. E. Nichols and A. P. Holmes, "Nonparametric permutation tests for functional neuroimaging: A primer with examples," *Human Brain Mapping*, vol. 15, no. 1, pp. 1–25, 2002.